JCAMECH

Four different types of a single drop dripping down a hole under gravity by lattice Boltzmann method

R. Haghani. H. A , M. H. Rahimian[§]

School of the Mechanical Engineering, College of Engineering University of Tehran, Tehran Iran.

Abstract

In this paper the dynamic of a droplet on a surface with a hole is investigated under gravitational effect by using lattice Boltzmann method. Incompressible two-phase flow with high density ratio proposed by Lee is considered. Cahn's theory is used to observe the wettability of the surface in contact with liquid and gas phases. Several parameters such as contact angle, surface tension and gravitational acceleration are studied to demonstrate their effects on the deformation of the droplet. To evaluate the results, the benchmark problems for equilibrium contact angle, capillary rise and Laplace law are conducted and a satisfactory agreement with analytical results is shown. Based on this study, four typical deformations of a droplet dripping down a hole can be observed; equilibrium drop on the top of the surface, equilibrium drop under the bottom of the surface, splashing and dripping of the drop. It is seen that at low Ohnesorge numbers the droplet deforms slightly and tends to retain its state. Moreover any increase in the Archimedes number magnifies the tendency to pass through the hole. Also, the relationship between the volume of the remaining droplet on the surface and Archimedes and Ohnesorge numbers is investigated. It is found that by increasing the Archimedes number, the volume of the remaining droplet on the surface reaches a constant value that is dependent on geometric parameters.

1. Introduction

In the recent years, lattice Boltzmann method has reached a great advancement for simulation of single and two-phase flow. Simple numerical coding and parallel processing on the one hand and possibility to simulate flow fields with complex boundaries on the other hand have encouraged most researchers to focus on this method more than the conventional CFD methods [1, 2]. Lattice Boltzmann simulations of two-phase flows have been used since 1990 in many works [3, 4]. Recently two-phase flow solvers using lattice Boltzmann method have been extended to the motion and deformation of the drops and bubbles [5, 6], liquid evaporation and steam condensation [7-9], and liquid jet impinging to a stagnant gas [10].

Droplet collision with a solid surface plays an important role in many industrial processes such as in the refinery and petrochemical reactors, printers,

---

[§] Corresponding anther Tell: +982161119930, Fax:+982188013029, Email: *rahimyan@ut.ac.ir*

surface covering, internal combustion engines, filters etc. For this purpose, dynamics of the droplet impact on a solid surface has been investigated by many researchers. Yarin Al et al. [11] have investigated a droplet collision and spread process on a dry surface. In their work the difference between the dynamic of a single droplet impact to a dry surface is compare to that of a train of droplets. Morton et al. [12] and Mukherjee et al. [13] investigated a droplet spreading on wet surfaces with a thin liquid film. Sikalo et al. [14-16] experimentally investigated the impact of the droplet on various horizontal and inclined surfaces and studied the relationships between several parameters such as the diameter of the wetting area on the solid surface and time variations of the contact angle. Haghani et al. [17] investigated the droplet collision on a surface with a hole. They observed that the dynamics of the droplet depends on several parameters such as the dimensionless height and the width of the hole and the droplet properties. Lunkat et al. [18] investigated the droplet dynamic on horizontal and inclined surfaces by the volume of fluid method (VOF) and examined the effects of wettability and inclined angle on the diameter of wetted spot. In this work, droplet impact on a surface with a hole is investigated. Moreover, the effects of the contact angle, surface tension and gravitational acceleration on the dynamics of the droplet are evaluated. It is shown that four regimes are seen in a droplet dripping down a hole, first when the drop remains on the top of the surface, second when the drop remains under the bottom of the surface, third when the drop breaks up and finally when the drop drips completely down the hole. All of these four cases are discussed in versus non-dimensional parameters.

2. Lattice Boltzmann method

In the lattice Boltzmann method, discrete Boltzmann equation with force term takes the following form [19]:

$$\frac{Df_\alpha}{Dt} = \left(\frac{\partial}{\partial t} + \mathbf{e}_\alpha.\nabla\right)f_\alpha =$$
$$-\frac{1}{\lambda}\left(f_\alpha - f_\alpha^{eq}\right) + \frac{1}{c_s^2}(\mathbf{e}_\alpha - \mathbf{u}).\mathbf{F}\Gamma_\alpha,$$
(1)

where $\mathbf{F}$ is obtained by determining the non-ideal gas effects takes the following form [19]:

$$\mathbf{F} = \nabla\rho c_s^2 - \nabla p_1 - C\nabla\mu(C) + \mathbf{F}_{ext}.$$
(2)

C is the concentration parameter and p_1 is the hydrodynamic pressure. External force ($\mathbf{F}_{ext}$) in this

work is the gravitational force and is calculated according to the following equation:

$$\mathbf{F}_{ext} = \left(\rho - \rho_g\right)g,$$
(3)

where g is the gravitational acceleration and the subscript g donates the gas phase. The thermodynamic pressure (p_0) is calculated from the Legendre equation

$$p_0 = C\frac{\partial E_0}{\partial C} - E_0,$$
(4)

where $E_0(C) \approx \beta C^2(C^2-1)$ is the bulk energy. $\mu = \mu_0 - \kappa\nabla^2 C$ is the chemical potential and μ_0 is the classical part of the chemical potential and the derivative of E_0 with respect to C,

$$\mu_0 = \frac{\partial E_0}{\partial C}.$$
(5)

The parameters β and κ are related to the surface tension σ and the interface thickness D.

$$\sigma = \frac{\sqrt{2\kappa\beta}}{6}, \quad D = \sqrt{\frac{8\kappa}{\beta}}.$$
(6)

Lee [20] used two distribution functions g and h for the pressure and composition evaluation equations, respectively

$$g_\alpha = f_\alpha c_s^2 + \left(p_1 - \rho c_s^2\right)\Gamma_\alpha(0),$$
(7)

$$h_\alpha = \left(\frac{C}{\rho}\right)f_\alpha,$$
(8)

where $\Gamma_\alpha(\mathbf{u}) = f_\alpha^{eq}/\rho$. Taking the total derivate $D_t = \partial_t + \mathbf{e}_\alpha.\nabla$ of g and h gives

$$\frac{\partial g_\alpha}{\partial t} + \mathbf{e}_\alpha.\nabla g_\alpha = -\frac{1}{\lambda}\left(g_\alpha - g_\alpha^{eq}\right) +$$
$$(\mathbf{e}_\alpha - \mathbf{u}).\begin{bmatrix}\nabla\rho c_s^2\left(\Gamma_\alpha - \Gamma_\alpha(0)\right) + \\ \left(-C\nabla\mu + \mathbf{F}_{ext}\right)\Gamma_\alpha\end{bmatrix},$$
(9)

$$\frac{\partial h_\alpha}{\partial t} + \mathbf{e}_\alpha . \nabla h_\alpha = -\frac{1}{\lambda}\left(h_\alpha - h_\alpha^{eq}\right)$$

$$+ \left(\mathbf{e}_\alpha - \mathbf{u}\right).\left[\nabla C - \frac{C}{\rho c_s^2}\left(\nabla p_1 + C\nabla \mu - \mathbf{F}_{ext}\right)\right]\Gamma_\alpha \qquad (10)$$

$$+ \nabla.\left(M\nabla \mu\right)\Gamma_\alpha,$$

where M is the mobility. The equilibrium distribution functions are given by

$$g_\alpha^{eq} = t_\alpha\left[p_1 + \rho c_s^2\left(\frac{\mathbf{e}_\alpha . \mathbf{u}}{c_s^2} + \frac{\left(\mathbf{e}_\alpha . \mathbf{u}\right)^2}{2c_s^2} - \frac{\left(\mathbf{u.u}\right)}{2c_s^2}\right)\right], \qquad (11)$$

$$h_\alpha^{eq} = t_\alpha C\left[1 + \frac{\mathbf{e}_\alpha . \mathbf{u}}{c_s^2} + \frac{\left(\mathbf{e}_\alpha . \mathbf{u}\right)^2}{2c_s^2} - \frac{\left(\mathbf{u.u}\right)}{2c_s^2}\right]. \qquad (12)$$

To facilitate the computation, the modified distribution functions $\bar{g}$ and $\bar{h}$ are applied:

$$\bar{g}_\alpha = g_\alpha + \frac{1}{2\tau}\left(g_\alpha - g_\alpha^{eq}\right) - \frac{\delta t}{2}\left(\mathbf{e}_\alpha - \mathbf{u}\right).\left[\nabla \rho c_s^2\left(\Gamma_\alpha - \Gamma_\alpha(0)\right) + \left(-C\nabla \mu + \mathbf{F}_{ext}\right)\Gamma_\alpha\right],$$

$$\qquad (13)$$

$$\bar{g}_\alpha^{eq} = g_\alpha^{eq} - \frac{\delta t}{2}\left(\mathbf{e}_\alpha - \mathbf{u}\right).\left[\nabla \rho c_s^2\left(\Gamma_\alpha - \Gamma_\alpha(0)\right) + \left(-C\nabla \mu + \mathbf{F}_{ext}\right)\Gamma_\alpha\right],$$

$$\bar{h}_\alpha = h_\alpha + \frac{1}{2\tau}\left(h_\alpha - h_\alpha^{eq}\right) - \frac{\delta t}{2}\left(\mathbf{e}_\alpha - \mathbf{u}\right).\left[\nabla C - \frac{C}{\rho c_s^2}\left(\nabla p_1 + C\nabla \mu - \mathbf{F}_{ext}\right)\right]\Gamma_\alpha,$$

$$\qquad (14)$$

$$\bar{h}_\alpha^{eq} = h_\alpha^{eq} - \frac{\delta t}{2}\left(\mathbf{e}_\alpha - \mathbf{u}\right).\left[\nabla C - \frac{C}{\rho c_s^2}\left(\nabla p_1 + C\nabla \mu - \mathbf{F}_{ext}\right)\right]\Gamma_\alpha.$$

By taking second-order integration in time, the LBE for the pressure and composition equations are summarized as follow:

$$\bar{g}_\alpha\left(\mathbf{x} + \mathbf{e}_\alpha \delta t, t + \delta t\right) - \bar{g}_\alpha\left(\mathbf{x},t\right) = -\frac{1}{\tau + 0.5}\left(\bar{g}_\alpha - \bar{g}_\alpha^{eq}\right)\left(\mathbf{x},t\right)$$

$$+ \delta t\left(\mathbf{e}_\alpha - \mathbf{u}\right).\left[\nabla \rho c_s^2\left(\Gamma_\alpha - \Gamma_\alpha(0)\right) + \left(-C\nabla \mu + \mathbf{F}_{ext}\right)\Gamma_\alpha\right]\Big|_{(\mathbf{x},t)}, \qquad (15)$$

$$\bar{h}_\alpha\left(\mathbf{x} + \mathbf{e}_\alpha \delta t, t + \delta t\right) - \bar{h}_\alpha\left(\mathbf{x},t\right) = -\frac{1}{\tau + 0.5}\left(\bar{h}_\alpha - \bar{h}_\alpha^{eq}\right)\left(\mathbf{x},t\right)$$

$$\qquad (16)$$

$$+ \delta t\left(\mathbf{e}_\alpha - \mathbf{u}\right).\left[\nabla C - \frac{C}{\rho c_s^2}\left(\nabla p_1 + C\nabla \mu - \mathbf{F}_{ext}\right)\right]\Gamma_\alpha\Big|_{(\mathbf{x},t)} + \delta t\nabla.\left(M\nabla \mu\right)\Gamma_\alpha\Big|_{(\mathbf{x},t)}.$$

Finally, the macroscopic variables can be calculated using the following equations:

$$C = \sum_\alpha \bar{h}_\alpha + \frac{\delta t}{2}\nabla.\left(M\nabla \mu\right),$$

$$\rho c_s^2 \mathbf{u} = \sum_\alpha \mathbf{e}_\alpha \bar{g}_\alpha - \frac{\delta t}{2}\left(C\nabla \mu + \mathbf{F}_{ext}\right), \qquad (17)$$

$$p_1 = \sum_\alpha \bar{g}_\alpha + \frac{\delta t}{2}\mathbf{u}.\nabla \rho c_s^2.$$

The density and relaxation time are given by

$$\rho(C) = C\rho_l + \left(1 - C\right)\rho_g,$$

$$\tau(C) = C\tau_l + \left(1 - C\right)\tau_g, \qquad (18)$$

where the subscripts of l and g donate liquid and gas phases, respectively.

Based on the Cahn's theory, the following boundary conditions are applied for presenting solid surface [21]:

$$\vec{\mathbf{n}}.\nabla \mu\big|_w = 0, \qquad (19)$$

$$\vec{\mathbf{n}}.\nabla C\big|_w = \sqrt{2\beta/\kappa\Omega}\left(C - C^2\right), \qquad (20)$$

where $\Omega=-cos(\theta^{eq})$ is the wetting potential.

3. Validation test

3.1. *Laplace law*

According to the Laplace law the pressure difference across the interface of a static drop is related to the surface tension via

$$\Delta p = p_{in} - p_{out} = \frac{\sigma}{R}, \tag{21}$$

where R is the radius of the drop at equilibrium. In order to verify the Laplace law, initially static drops with different radius are generated in the middle of the computational domain. The numerical results are compared with the theoretical solution (Eq. 21) in Fig. 1. It can be seen that the numerical results are in satisfactory agreement with the theoretical values.
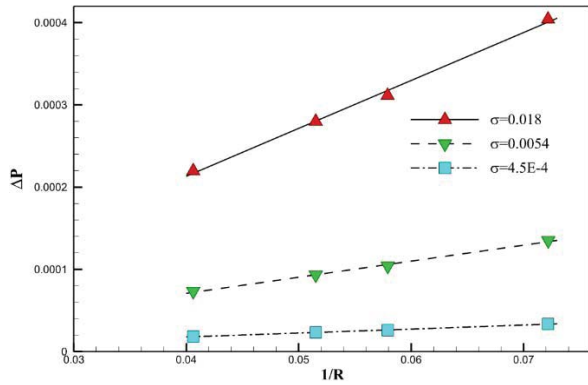

Fig. 1 Verification of Laplace Law for three different values of surface tension

3.2. *Partial wetting boundary*

To verify the numerical solution equilibrium contact angle, a droplet initiates moving to the surface with the different contact angles. The numerical equilibrium contact angle and the theoretical solution ($\Omega=-cos(\theta^{eq})$)) are compared in Fig. 2 in the range of contact angle from $10°$ to $170°$. As it can be seen, the numerical results are in a good agreement with the theoretical values.

4. Drop dripping down a hole

4.1. *Computational setup*

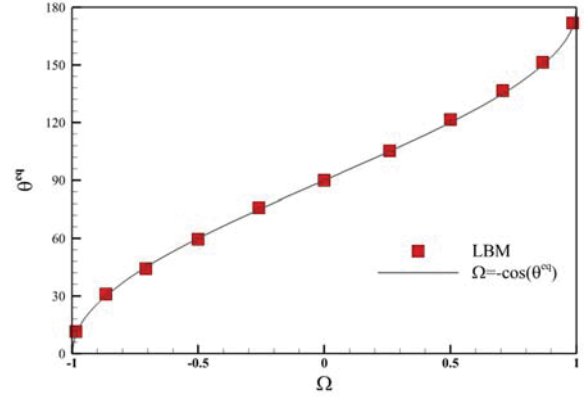In this section, a drop dripping down a hole is

Fig. 2: The simulated equilibrium contact angle vs. the theoretical solution

considered. Fig. 3 is a schematic of this problem. A two dimensional liquid drop with a diameter of 50lattice cells is generated tangent to the surface. A 200×300 computational domain for a D2Q9 lattice is implemented. The boundary condition for solid surface is partial wetting boundary while periodic boundary condition is used in vertical and horizontal directions. The ratio of the wall thickness to the drop diameter ($h^* = h/D$) and the hole diameter to the drop diameter ($d^* = d/D$) are fixed 0.1 and 0.6, respectively.

The results are presented in terms of Archimedes and Ohnesorge numbers based on drop properties.

$$Oh = \frac{\mu_d}{\sqrt{\rho_d D \sigma}} \quad \begin{array}{l} \text{Ohnesorge} \\ \text{number} \end{array} \tag{22}$$

$$Ar = \frac{\sqrt{gD^3}}{\nu_d} \quad \begin{array}{l} \text{Archimedes} \\ \text{number} \end{array} \tag{23}$$

where D is the drop diameter, g is the gravitational acceleration, ρ_d is the density of the drop, and μ_d is the dynamic viscosity of the drop.

$$Oh = \frac{\mu_d}{\sqrt{\rho_d D \sigma}} \quad \begin{array}{l} \text{Ohnesorge} \\ \text{number} \end{array} \tag{22}$$
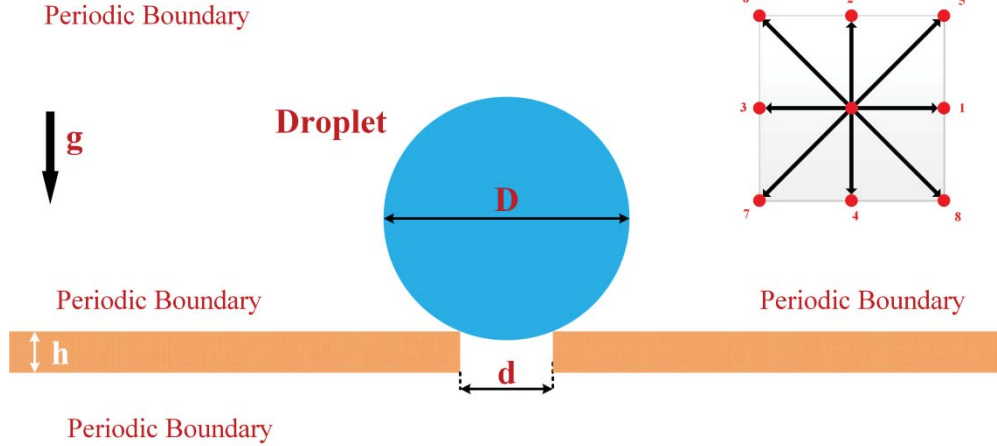
Fig. 3: Schematic representation of the domain

$$Ar = \frac{\sqrt{gD^3}}{v_d} \qquad \text{Archimedes number} \qquad (23)$$

where D is the drop diameter, g is the gravitational acceleration, ρ_d is the density of the drop, and μ_d is the dynamic viscosity of the drop.

The dimensionless time is defined by,

$$t^* = T \bigg/ \left(\frac{\mu_d D}{2\sigma} \right), \qquad (24)$$

where T is the number of iterations.

4.2. Mesh independency

At first, the mesh independancy was performed for one case. As shown in Fig. 3, the shapes at two dimensionless times for two grids with 200×300 and 400×600 lattice cells are in agreement with one another. Hence, in order to reduce computation time, a 200×300 grid has been selected for computational domain.

4.3. Density ratio and dynamic viscosity ratio

To study the effects of the density ratio, ρ_l/ρ_g , and the dynamic viscosity ratio, μ_l/μ_g , the properties of the drop are fixed and the density and dynamic viscosity of the gas phase are changed. The effects of the density and dynamic viscosity ratio on dynamic behavior of the drop are shown in Fig. 4a and Fig. 4b,
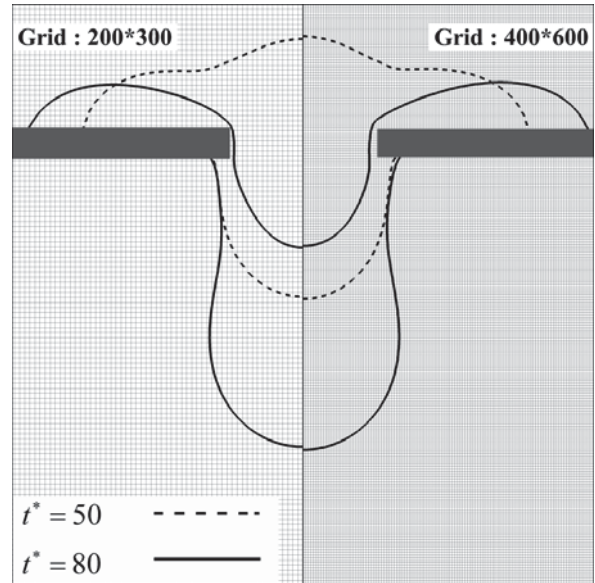

Fig. 3: Grid independency at $t^* = 50$, $t^* = 80$ ($Ar = 243.03$, $Oh = 0.0133$, $\theta^{eq} = 60°$) respectively.

As shown in Fig. 4a, the effects of different density ratios of 100 and 500 at $t^* = 260$ are not very significant on their shapes. However, at the density ratio of 10, the drop has a major difference at vertical position and its shape. It is known that the gravity force is proportional to the density difference, $\Delta \rho$, assuming $\rho_l = 1$, $\Delta \rho$ for the density ratios (ρ_l/ρ_g) of 10, 100, 500 is respectively 0.9, 0.99 and 0.998. Thus, by increasing the density ratio, the gravity force tends to a constant number and a fixed deformation of the drop occurs. To investigate the effects of dynamic viscosity on the drop behavior, three dynamic viscosity ratios (10, 20 and 33.33) are evaluated. As shown in Fig. 4b, there is a little difference at dynamic viscosity

ratios of 20 and 33.33. When the dynamic viscosity ratio is large ($\mu_l/\mu_g = 33.33$), the resistance of the gas phase is low enough to allow great spreading of the drop on the surface. Thus, breakup of the drop occurs later and the drop has a higher vertical position than a drop with lower dynamic viscosity ratio. Also, the remaining droplet volume on the surface in this case is greater. Therefore, in the rest of the simulations, $\rho_l/\rho_g = 100$ and $\mu_l/\mu_g = 20$ are selected to see the effects of other non-dimensional parameters.
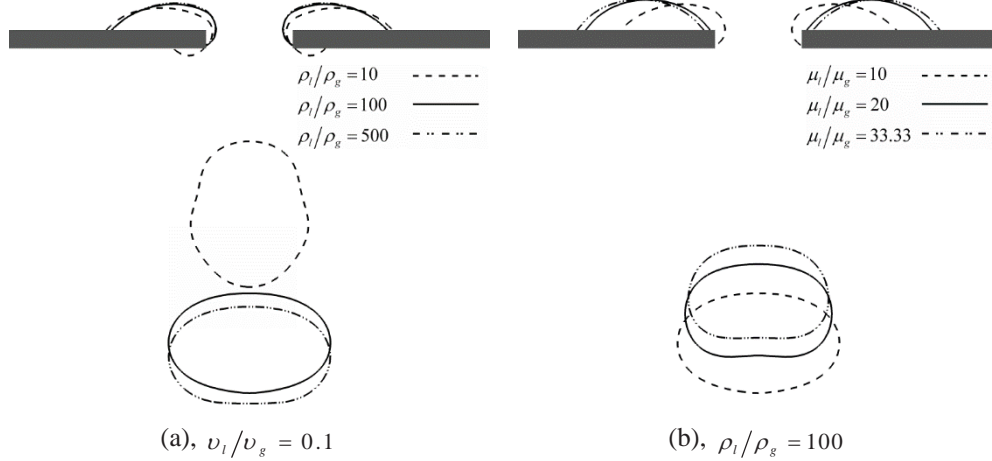

$$\rho_l/\rho_g = 10 \quad \text{------}$$
$$\rho_l/\rho_g = 100 \quad \text{———}$$
$$\rho_l/\rho_g = 500 \quad \text{-- - -- -}$$

$$\mu_l/\mu_g = 10 \quad \text{------}$$
$$\mu_l/\mu_g = 20 \quad \text{———}$$
$$\mu_l/\mu_g = 33.33 \quad \text{-- - -- -}$$

(a), $\upsilon_l/\upsilon_g = 0.1$ (b), $\rho_l/\rho_g = 100$

Fig. 4: Effects of (a) the density ratio (b) the dynamic viscosity for $Ar = 237.17$, $Oh = 0.0105$, $t^* = 260$, $\theta^{eq} = 60°$

4.4. *Shape and position evolution*

The dynamic behavior of a drop moving on a surface with a hole, is investigated in this section. Shape and deformation time of the drop from the initial state to the final state depend on the properties of the drop and surface. These properties include surface tension, equilibrium contact angle, density and viscosity ratios, and gravitational acceleration. Based on our numerical results, we find that for different Ohnesorge numbers, Archimedes numbers, and equilibrium contact angles, the dynamic behavior of the drop can be divided into four states; equilibrium on the top of the surface, equilibrium under the bottom of the surface, splashing and dripping. Results are shown in Fig. 6 for five equilibrium contact angles; $\theta^{eq} = 30°$, $60°$, $90°$, $120°$, $150°$, and different Archimedes and Ohnesorge numbers.

When the contact angle is equal to 30 degrees, the dynamics of the drop is divided into three types: equilibrium on the top of the surface (Region 1), equilibrium under the bottom of the surface (Region 2) and splashing (Region 3). While the Archimedes number increases, the gravitational acceleration increases and the drop has greater tendency to pass through the hole. Thus, at a constant Ohnesorge, by increasing the Archimedes number the drop behavior changes from region 1 to region 2 and then to region 3, respectively. By increasing the contact angle to 60 degrees (Fig. 6b), a new region that is called the dripping region (Region 4) is seen and the equilibrium

at the bottom of the surface (Region 2) is shrunk due to the reduction of the force between the drop and the surface. At $\theta^{eq} = 30°$, the drop is spread on the surface along the horizontal direction more than the other contact angles and due to this reason the surface tension overcomes the gravity. Thus, at the contact angle of 30 degrees, the dripping mode (Region 4) has not been observed.

When the contact angle is equal to 90 degrees (Fig. 6c), the equilibrium at the bottom of the surface, (Region 2), can be seen at low Ohnesorge numbers. As shown in Fig. 6c, the drop on the surface has contact angle of 90 degrees (Region 1). At contact angle of more than $90°$, the surface is hydrophobic and region (2) will not be observed. Therefore, the dripping drop region (Region 4) is expanded.

At $\theta^{eq} = 120°$ (Fig. 6d), the remaining droplets on the surface that have velocity towards the center of the hole continue their motion and drop down the hole. So, we consider this region different from the splashing region with remaining droplets up the surface (Region 3). This is considered the splashing region with dripping drops (Region 5). At $\theta^{eq} = 150°$ (Fig. 6e) as $\theta^{eq} = 120°$, region 5 is replaced by region 3. By increasing the contact angle from 120 degrees to 150 degrees, the hydrophobic intensity increases and it appears to shrink the dripping zone (Region 4) and expand regions 1 and 5. A comparison between Fig. 6d and Fig. 6e confirms the validity of this statement.
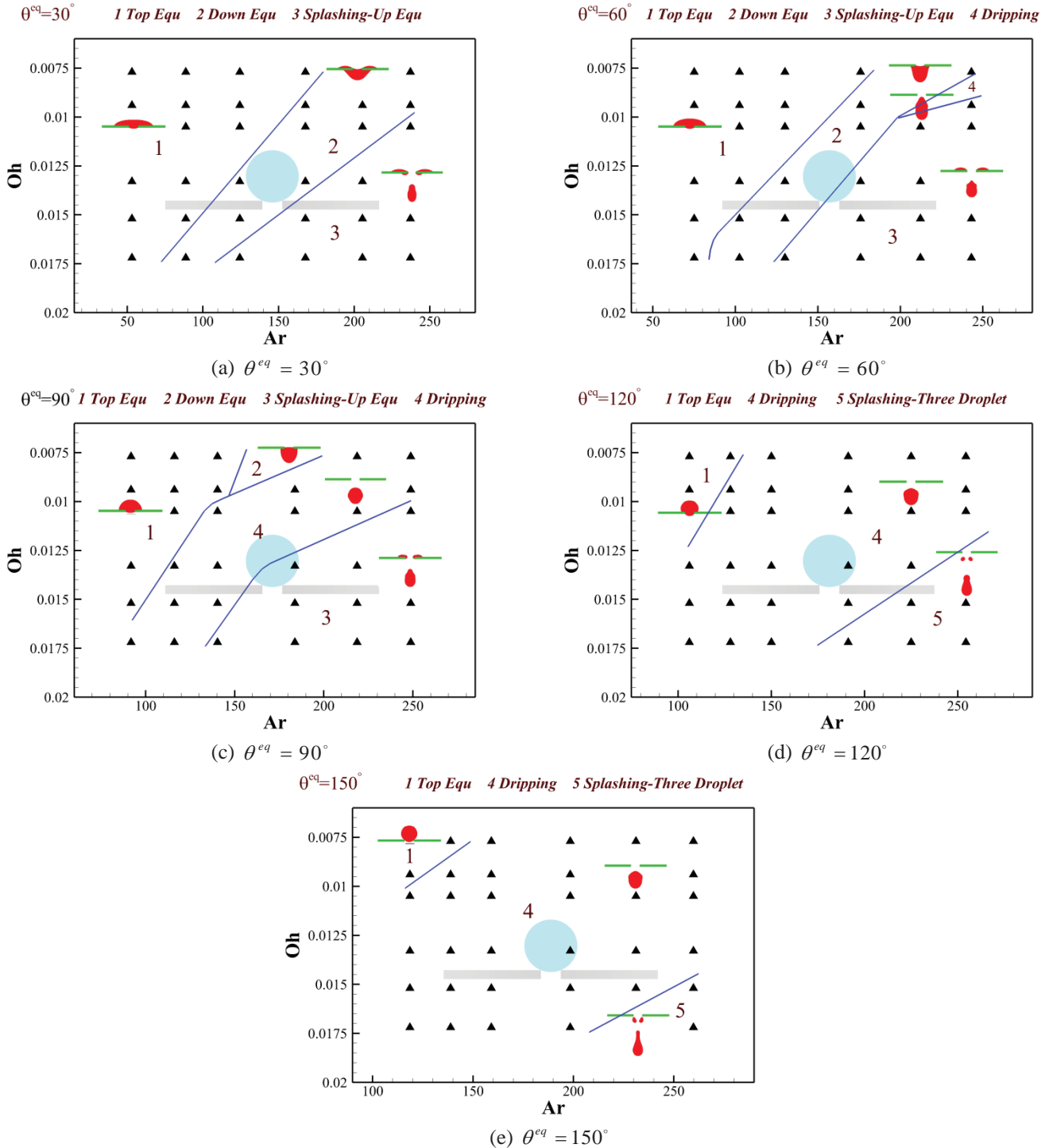
(a) $\theta^{eq} = 30°$

(b) $\theta^{eq} = 60°$

(c) $\theta^{eq} = 90°$

(d) $\theta^{eq} = 120°$

(e) $\theta^{eq} = 150°$

Fig. 6: Dynamic behavior of the drop at different Archimedes and Ohnesorge numbers and, equilibrium contact angle ($\rho_l / \rho_g = 100$ and $\mu_l / \mu_g = 20$).

4.5. *Volume of the remaining droplets on the surface*

The volume of the remaining droplets on the surface at $\theta^{eq} = 60°$ for different Ohnesorge and Archimedes numbers is plotted in Fig. 7. V^* is defined as ratio of the volume of the droplets remaining on the surface to the initial volume of the drop.
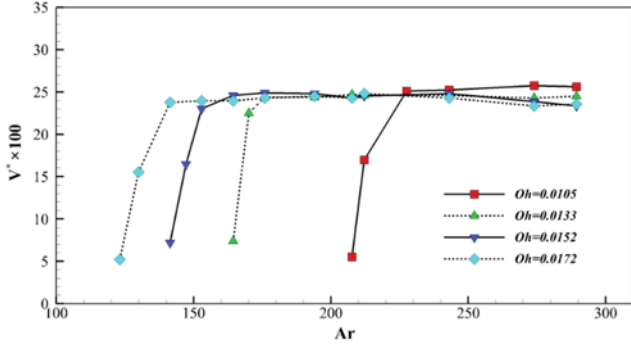
Fig. 7: Variations of V^* versus different Archimedes numbers at different Ohnesorge numbers.

By increasing Archimedes number, gravitational acceleration will be increased, thus a greater gravity force is applied to the drop and the velocity of its center increases. In this case, the drop does not have enough time to overcome the surface tension force, thus it will be divided into smaller droplets. With further increase in the Archimedes number, the effect of the drop velocity on V^* is decreased and V^* reaches a constant value.

As shown in Fig. 7, at any constant Ohnesorge number, by increasing Archimedes number, the dimensionless volume, V^*, reaches a constant value. The dimensionless value for different Ohnesorge numbers is the same and it only depends on the ratio of the hole diameter to initial drop diameter, $d^* = d/D$, that is approximately equal to 24.5 for $d/D = 0.6$.

To study the influence of the dimensionless diameter of the hole on the dimensionless volume, Ohnesorge and Archimedes numbers are varied at different d^*. The results for different d^*s are shown in Fig. 8. By decreasing d^*, we observe that the dimensionless volume is increased due to the increase of the resistant force applied by the hole. Also, the dripping drop has a higher position in vertical direction at the same time. The slope of the lines at smaller d^* is higher than greater d^* showing that the effect of d^* on V^* can be weakened by increasing d^*.
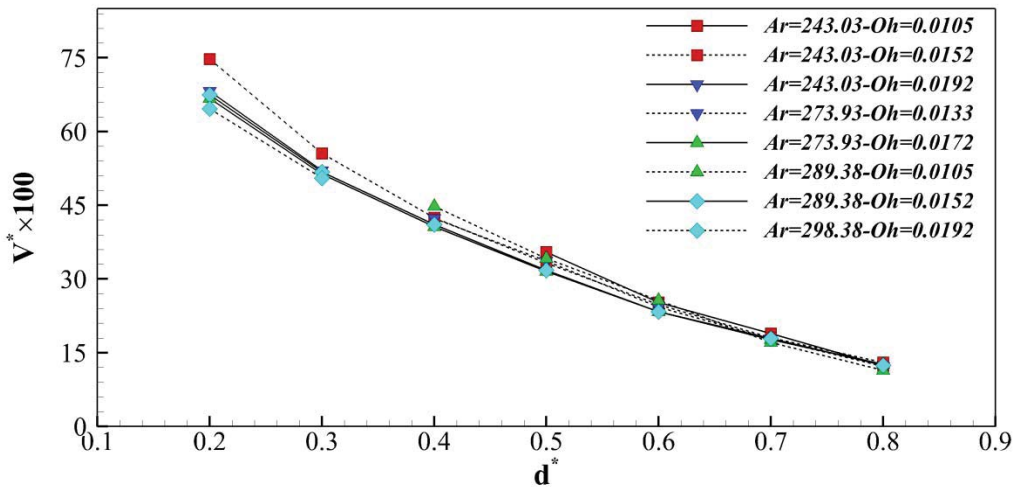

Fig. 8: Variations of V^* versus the dimensionless diameter d^* for different Archimedes and Ohnesorge numbers at $\theta^{eq} = 60°$

4.6. *Velocity field*

Finally, the streamlines inside and outside of the droplet are shown in Fig. 9. The streamlines are plotted form the point of view of the observer who moves with the average velocity of the drop. Note that the presented dimensionless times are in different values because a number of times is required for the drop to reach equal position at different Archimedes and Ohnesorge numbers. To investigate the effects of Ohnesorge number, Figs. 9a-d are compared. By increasing Ohnesorge number, the tendency of the drop for retaining its own state is reduced, and it passes through the hole with a greater velocity. Hence, the surrounding flow is less affected by the drop motion and the streamlines become more uniform. Also, at the same vertical position, the drop with greater Ohnesorge number has lower dimensionless time. In Fig. 9c, the drop decay at higher Ohnesorge number induces two vortices that are formed on the back side of the drop. Fig. 9d is plotted for zero surface tension that has great deformation and reaches the same position at lower dimensionless time ($t^* = 0.018$).

The effects of Archimedes numbers are plotted in Figs 9b, 9e, and 9f at the same Ohnesorge number ($Oh = 0.0133$). At a lower Archimedes number (Fig. 9e), consequently, lower gravitational acceleration, the

vertical velocity of the drop is low and the drop reaches the same position at higher t^* ($t^* = 180$) and the flow field at the back of the drop does not have any vortices. By increasing the Archimedes number to 212.13 (Fig. 9b), two vortices are generated at the edge of the remaining droplets on the surface. At the highest Archimedes value (Fig. 9f), a pair of vortices is generated behind the drop and two relatively big vortex rings are created beside the drop.
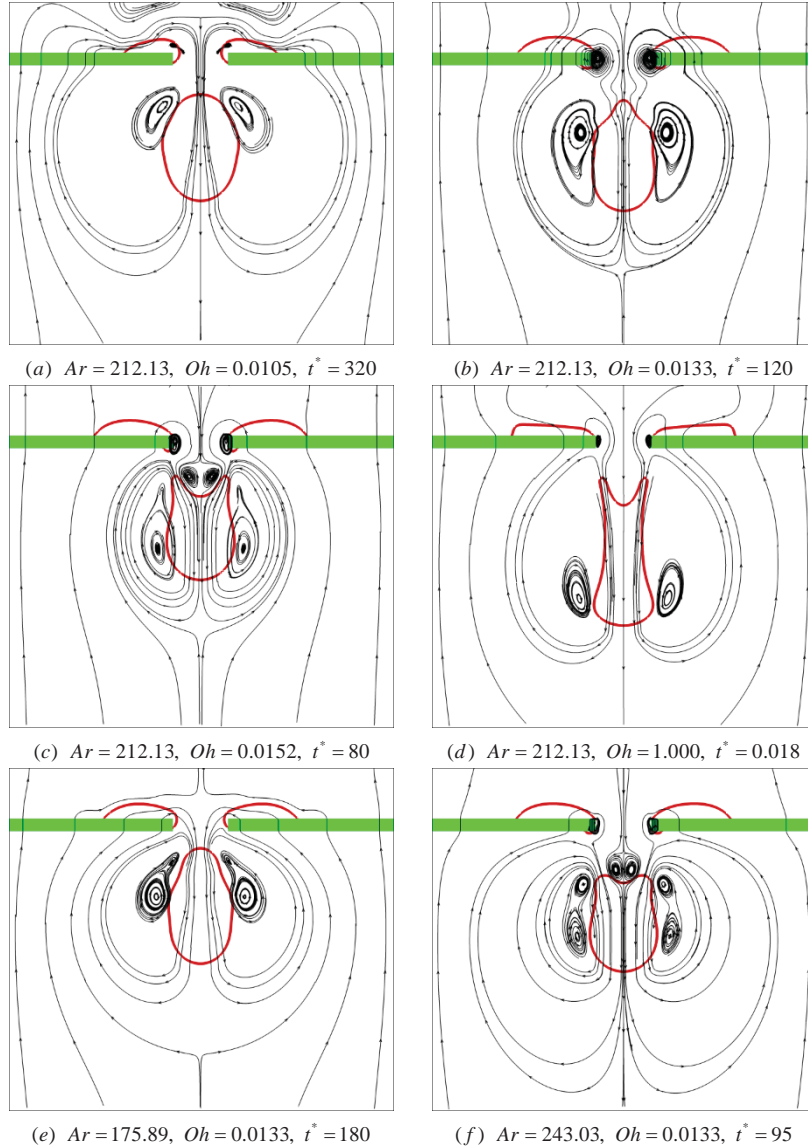

(a) $Ar = 212.13$, $Oh = 0.0105$, $t^* = 320$

(b) $Ar = 212.13$, $Oh = 0.0133$, $t^* = 120$

(c) $Ar = 212.13$, $Oh = 0.0152$, $t^* = 80$

(d) $Ar = 212.13$, $Oh = 1.000$, $t^* = 0.018$

(e) $Ar = 175.89$, $Oh = 0.0133$, $t^* = 180$

(f) $Ar = 243.03$, $Oh = 0.0133$, $t^* = 95$

Fig. 9: streamlines inside and outside the dripping drop. The contours (shown in red) denote the interface

5. Conclusions

A comprehensive study of drop dynamics on the surface with a hole was performed based on the lattice Boltzmann method. The effects of the contact angle, surface tension, gravitational acceleration, density ratio, viscosity ratio and geometric parameters were investigated in a 2D computational domain. It was shown that the dynamic viscosity ratio has more effects on the dynamics of the drop than the density ratio does. Based on the results, the dynamic of the drop was divided into four typical deformations. It was shown that by increasing the Archimedes number, the dimensionless time for reaching the same position is reduced. By increasing the Ohnesorge number, surface tension decreases resulting in higher deformation of the drop. The streamlines were plotted to display vortices around the drop. It was shown that the number, shape and size of the vortices are dependent on the Archimedes and Ohnesorge numbers. Also, the

ratio of the remaining drop volume on the surface to the initial volume were calculated, and it was presented that by increasing the Archimedes number, this ratio reaches a constant value that is dependent on the geometric parameters such as the ratio of the hole diameter to the initial drop diameter.

References

[1] M. C. Sukop and D. T. Thorne, *Lattice Boltzmann Modeling: An introduction for Geoscientists and Engineers*. Berlin: Springer, 2005.

[2] H. X and L. Ls, "A priori derivation of the lattice Boltzmann equation," *Phys Rev E,* vol. 55, p. R6333, 1997.

[3] S. Chen and G. D. Doolen, "Lattice Boltzmann method for fluid flows," *Ann. Rev. Fluid Mech. ,* vol. 30, pp. 329-364, 1998.

[4] S. Succi, *The Lattice Boltzmann Equation for Fluid Dynamics and Beyound*, 2001.

[5] A. Fakhari and M. H. Rahimian, "SIMULATION OF AN AXISYMMETRIC RISING BUBBLE BY A MULTIPLE RELAXATION TIME LATTICE BOLTZMANN METHOD," *International Journal of Modern Physics B,* vol. 23, 2009.

[6] M. Taghilou and M. H. Rahimian, "Investigation of two-phase flow in porous media using lattice Boltzmann method," *Computers & Mathematics with Applications,* vol. 67, pp. 424–436, 2014.

[7] H. Safari, M., M. H. Rahimian, M Krafczyk , "Consistent simulation of droplet evaporation based on the phase-field multiphase lattice Boltzmann method," Physical Review E 90 (3), 033305, 2014.

[8] A. Begmohammadi, M. H. Rahimian, M. Farhadzadeh, and M. A. Hatani, "Numerical simulation of single-and multi-mode film boiling using lattice Boltzmann method," *Computers & Mathematics with Applications,* vol. 71, pp. 1861–1874, 2016.

[9] M. A. Hatani, M. Farhadzadeh, and M. H. Rahimian, "Investigation of vapor condensation on a flat plate and horizontal cryogenic tube using lattice Boltzmann method," *International Communications in Heat and Mass Transfer,* vol. 66, pp. 218–225, 2015.

[10] H. Amirshaghaghi, M. H. Rahimian, and H. Safari, "Application of a two phase lattice Boltzmann model in simulation of free surface jet impingement heat transfer " *International Communications in Heat and Mass Transfer,* vol. 75, pp. 282–294, 2016.

[11] A. L. Yarin and D. A. Weiss, "Impact of drops on solid surfaces: self-similar capillary waves, and splashing as a new type of kinematic discontinuity," *J Fluid Mech,* vol. 283, pp. 283-141, 1995.

[12] D. Morton, M. Rudman, and L. Jong-Leng, "An investigation of the flow regimes resulting from splashing drops," *Phys Fluid,* vol. 12, 2000.

[13] S. Mukherjee and J. Abraham, "Lattice Boltzmann simulations of two-phse flow with high density ratio in axially symmetric geometry," *Phys Rev E,* vol. 75, p. 026701, 2007.

[14] S. Sikalo, M. Marengo, C. Tropea, and E. N. Ganic, "Analysis of impact of droplets on horizontal surfaces," *Exp. Therm. Fluid Sci.,* vol. 25, pp. 503-510, 2005.

[15] S. Sikalo, C. Tropea, and E. N. Ganic, "Dynamic wetting angle of spreading droplet," *Exp. Therm. Fluid Sci.,* vol. 29, pp. 795-802, 2005.

[16] S. Sikalo, C. Tropea, and E. N. Ganic, "Impact of droplets onto inclined sufraces," *J. Colloid Interf. Sci.,* vol. 286, pp. 661-669, 2005.

[17] R. Haghani, M. H. Rahimian, and M. Taghilou, "LBM Simulation of a Droplet Dripping Down a Hole," *Eng. App. Comp. Fluid Mech.,* vol. 7, pp. 461-470, 2013.

[18] S. F. Lunkad, V. V. Buwa, and K. D. P. Nigam, "Numerical simulations of drop impact and spreading on horizontal and inclined surface," *Chem. Eng. Sci.,* vol. 62, pp. 7214-7224, 2007.

[19] X. He, X. Shan, and G. D. Doolen, "Discrete Boltzmann equation model for nonideal gases," *Physical Review E,* vol. 57, pp. R13--R16, 1998.

[20] T. Lee, "Effects of incompressibility on the elimination of parasitic currents in the lattice Boltzmann equation method for binary fluids," *Com. Math. App.,* vol. 58, pp. 987-994, 2009.

[21] T. Lee and L. Liu, "Lattice Boltzmann simulations of micron-scale drop impact on dry surfaces," *J. Com. Phy.,* vol. 229, pp. 8045-8063, 2010.